Gaseous CO2 behaviour during water displacement in a sandstone core sample

Gaseous CO_2 Behaviour during Water Displacement in a Sandstone Core Sample

Ebraheam Al-Zaidi[a], Katriona Edlmann[b], Xianfeng Fan*[a]

[a] Institute for Materials and Processes, School of Engineering, The King's Buildings, The University of Edinburgh, Mayfield Road, Edinburgh, EH9 3JL, United Kingdom

[b] School of Geoscience, Grant Institute, The King's Buildings, The University of Edinburgh, James Hutton Road, Edinburgh EH9 3FE, United Kingdom.

* Corresponding author. Tel.: +44 0 131 6505678; fax: +44 0131 6506551. E-mail address: x.fan@ed.ac.uk

Abstract: CO_2 injection into subsurface formations involves the flow of CO_2 through a porous medium that also contains water. The injection, displacement, migration, storage capacity and security of CO_2 is controlled mainly by the interfacial interactions and capillary, viscous, and buoyancy forces which are directly influenced by changes in subsurface conditions of pressure and temperature; the impact of bouncy forces is assumed negligible during this study. In this study, gaseous CO_2 is injected into a water-saturated sandstone core sample to explore the impact of fluid pressure (40-70 bar), temperature (29-45 °C), and CO_2 injection rate (0.1-2 ml/min) on the dynamic pressure evolution and displacement efficiency. This study highlights the impact of capillary or viscous forces on the two-phase flow characteristics and shows the conditions where capillary or viscous forces become more influential. The results reveal a moderate to considerable impact of the parameters investigated on the differential pressure profile, endpoint CO_2 relative permeability (K_{rCO2}^{max}), and irreducible water saturation (S_{wr}). Overall, the increase in fluid pressure, temperature, and CO_2 injection rate cause an increase in the maximum and final differential pressures, an increase in the K_{rCO2}^{max}, a reduction in the S_{wr}. S_{wr} was in the range of around 0.38-0.45 while K_{rCO2}^{max} was less than 0.25. The data show a significant influence for the capillary forces on the pressure and production behaviour. The capillary forces produce high oscillations in the pressure and production data while the increase in viscous forces impedes the appearance of these oscillations. The appearance and frequency of the oscillations depend on the fluid pressure, temperature, and CO_2 injection rate but to different extents.

1 Introduction

Carbon capture and storage (CCS) is regarded as one of the most promising techniques that can deal effectively with the increasing emissions of anthropogenic CO_2 into the atmosphere due to fossil fuel burning and other human activities (Bachu, 2001; Hangx et al., 2013; Kazemifar et al., 2015). The captured CO_2 can be sequestered in deep saline aquifers, depleted or abandoned oil and gas reservoirs (Delshad et al., 2010; Gozalpour et al., 2005; Kaveh et al., 2012), or unmineable coal bed seams (Kaveh et al., 2012; Plug and Bruining, 2007) to enhance recovery from hydrocarbon reservoirs, increase methane production from coal beds, or extract geothermal heat from subsurface formations (Kaveh et al., 2012; Tutolo et al., 2015). Figure 1 presents a summary of the pressure and temperature ranges at which saline aquifers are found underground and highlights that CO_2 can exist in a gaseous, liquid or supercritical phase (Bachu, 2000; Espinoza and Santamarina, 2010; Frailey et al.; Nourpour Aghbash and Ahmadi; Saraji et al., 2014; Sohrabi et al.).

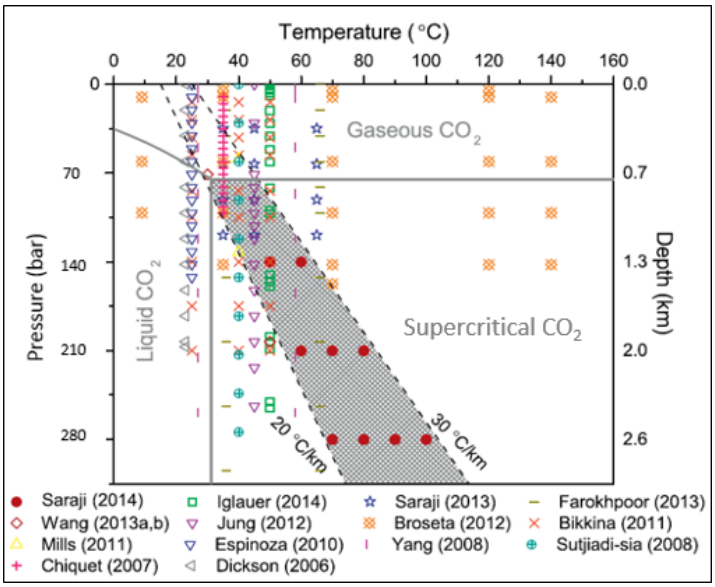

Figure 1: The pressure and temperature ranges at which saline aquifers are found underground (Saraji et al., 2014). This study is conducted under pressure ranged from 40 to 70 bar and temperature ranged from 29 to 45 °C.

During CO_2 injection in subsurface formations, the bulk of the injected CO_2 (as a non-wetting fluid) will displace the formation water (as a wetting fluid) in an immiscible displacement (Basbug et al., 2005; Herring et al., 2014b). The displacement of the injected CO_2 depends on a number of parameters,

namely, the interfacial interactions (e.g. interfacial tension and wettability), solubility of CO_2 in formation water, densities and viscosities of fluids present, petrophysical properties of the subsurface formation, injection rate and its duration , and more importantly on the capillary and viscous forces (Cinar and Riaz, 2014; Duan and Sun, 2003; Pentland et al., 2011b; Trevisan et al., 2017). The capillary forces at the CO_2-water interface are of considerable importance in determining the nature of the flow through pores (Roof, 1970). Any change in subsurface conditions of pressure and temperature will have a significant impact on the interfacial interactions (Espinoza and Santamarina, 2010; Liu et al.; Plug and Bruining, 2007; Yang et al., 2007), the viscous forces due to the change in viscosity (Bachu and Bennion, 2008b) and the capillary forces. The change in interfacial interactions, and viscous and capillary forces due to the change in underground conditions will have a considerable influence on the capillary pressure, relative permeability (Alkan et al., 2010), pore-scale fluid distribution (Al-Menhali and Krevor, 2014), CO_2 injection, fluid migration, capacity and long-term fate of CO_2 storage in saline aquifers (Levine et al., 2011; Saraji et al., 2013; Wang et al., 2015), CO_2-enhanced oil and gas recovery processes (Gozalpour et al., 2005; Qi et al., 2010). According to Salimi et al., the change in capillary pressure, due to the change in the operational conditions, can have a direct influence the CO_2-storage capacity and the heat recovery due to its impact on the solubility and density of both CO_2 and water (Salimi et al., 2012). Thus, it is of utmost importance to have a deep insight into the dynamic behaviour of CO_2 under different operational conditions.

CO_2 has been used in the oil industry for a long time, in particular, to increase productivity through Enhanced Oil Recovery (EOR), and extensive research has been undertaken describing multi-phase flow properties of CO_2-oil systems (Bahralolom et al., 1988). On the other hand, much less laboratory investigations have been done for CO_2-water (brine) systems (Perrin and Benson, 2010). Those published have mainly focused on CO_2 wettability (Al-Menhali and Krevor, 2014; Bikkina, 2011; Farokhpoor et al., 2013a; Kaveh et al., 2012; Sakurovs and Lavrencic, 2011; Saraji et al., 2013), CO_2-water (brine) interfacial tension (Aggelopoulos et al., 2010; Bachu and Bennion, 2008b, 2009; Busch and

Müller, 2011; Chiquet et al., 2007; Li et al., 2012; Yu et al., 2012), relative permeability (Bachu, 2013; Krevor et al., 2015; Liu et al.; Perrin et al., 2009) and capillary pressure (Busch and Müller, 2011; Pini et al., 2012; Plug and Bruining, 2007). Cinar and Riaz showed that much of the research has been directed to investigate the fluid properties rather than studying the multiphase flow properties of the CO_2-water systems (Cinar and Riaz, 2014).

The limited investigations of the multiphase flow characteristics of CO_2-water (brine) systems have involved laboratory experiments (Jobard et al., 2013), computational modelling (Jobard et al., 2013; Ma et al., 2013; Xu et al., 2011), and field scale projects (Wang et al., 2015). The CO_2-water (brine) investigations included core flooding displacements performed at liquid, supercritical and gaseous CO_2 conditions. Current literature survey of the CO_2-water (brine) multiphase flow experiments showed that most of these experiments were supercritical (Sc) CO_2-brine (water) displacements studies, which were performed on various porous media such as core samples (Berg et al., 2013; Edlmann et al., 2013), micromodels (Cao et al., 2016), and packed beds of glass beads (Song et al., 2012; Suekane et al., 2005). In these studies related to supercritical CO_2 migration, researchers have examined various parameters such as relative permeability curves (Berg et al., 2013; Chang et al., 2013; Krevor et al., 2013; Suekane et al., 2005; Suenaga and Nakagawa, 2011), capillary pressure curves (Herring et al., 2014a; Wang et al., 2013), CO_2 residual saturation and distribution (Alemu et al., 2011; Chang et al., 2013; Herring et al., 2014a; Pentland et al., 2011a; Saeedi et al., 2011; Suekane et al., 2005), heterogeneity impact (Ott et al., 2015; Perrin and Benson, 2010; Shi et al., 2011; Wang et al., 2013), water displacement efficiency (Cao et al., 2016), mass transfer (Berg et al., 2013), and formation dry-out (Ott et al., 2011). Some liquid (L) CO_2-water (brine) core flooding displacements were conducted to investigate the multiphase flow characteristics of CO_2-water-porous media (Manceau et al., 2015), CO_2 residual saturation and distribution (Alemu et al., 2011), and pore-scale heterogeneity (Zhang et al., 2011).

On the other hand, very scarce data was found regarding gaseous (G) CO_2 injection into water (brine) saturated porous systems (Islam et al., 2013; Jiang et al., 2017; Lassen et al., 2015; Yu et al., 2014).

Even though liquid and supercritical CO_2 injection is more efficient, the dynamic behaviour of gaseous CO_2 in reservoir rock is necessary information, particularly considering that many potential saline storage aquifers are within temperature and pressure conditions of the gaseous CO_2 phase (Figure 1) and that any leakage of CO_2 from deeper storage would inevitably result in a phase change to a gaseous CO_2 state (Edlmann et al., 2016; Miocic et al., 2016). The existing GCO_2-water experiments were designed to investigate the crossover zone of flow regimes, impact of capillary number, CO_2 injection rates and permeability on displacement efficiency. Islam et al. conducted GCO_2-water experiments at 1 bar and 25 °C using a vertical Hele-Shaw cell filled with micro-beads to investigate the crossover zone from capillary to viscous to fracture fingering. They observed that all the three fingering patterns can occur in the cell but at different heights (Islam et al., 2013). Jiang et al. performed both immiscible and miscible drainage GCO_2-water displacements inside a packed bed filled with quartz glass beads to have a better understanding of the two-phase flow characteristics inside porous media. The experiments were conducted at CO_2 injection rates varying from 0.01 to 3 ml/min and at 60 bar and 24.85 °C. They observed that: (I) at low CO_2 injection rates, the CO_2 dissolution increases; (II) the increase in glass beads diameter (i.e. higher permeability) leads to a decrease in the capillary forces (Jiang et al., 2017). Yu et al. conducted immiscible drainage GCO_2-water displacements at 60 bar and 24.85 °C inside a packed bed of glass beads (0.2 mm diameter) to study the impact of the capillary number on displacement efficiency. They noticed that the increase in the capillary number, when it is between 10^{-11} and 10^{-10}, results in a sharp reduction in the residual water saturation as a result of increasing the impact of the viscous forces (Yu et al., 2014).

Despite the considerable research on the CO_2–water (brine) systems and its practical importance, the analysis of the pressure data in core flooding has been widely overlooked (Rezaei and Firoozabadi, 2014). To the authors' best knowledge, there is no detailed investigation into the dynamic pressure evolution and displacement efficiency of gaseous CO_2 during its injection into a water saturated core sample. In this paper, laboratory dynamic drainage experiments were performed by injecting pure CO_2 into the deionised water-saturated sandstone core sample to investigate the impact of fluid pressure,

temperature, and CO_2 injection rate on the differential pressure profile, water production, and endpoint effective and relative permeabilities of CO_2. This study also highlights the impact of capillary and viscous forces on the pressure and production data as well as shows the conditions at which capillary or viscous forces become more influential**.** During these dynamic displacements, the transient pressure at the inlet and outlet sides of the core and the transient outflow rates of water and CO_2 were measured and analyzed. The endpoint water saturations of CO_2 and water were also calculated.

2 Materials

A sandstone core sample from the Guillemot A Field in the North Sea was used to perform the unsteady state GCO_2-water drainage experiments. The core sample has a diameter of 2.54 cm and a length of 7.62 cm. The average porosity and absolute water permeability of the core sample were about 14% and 15.8 millidarcys, respectively. This study is one in a series, thus the core sample description, the experimental setup and the CO_2-water displacement procedures can be seen in our recent publication (Al-Zaidi et al., 2018).

3 Results and discussion

To gain a deep insight into the dynamic behaviour of GCO_2-water drainage displacements under various fluid pressure, temperature, and injection rate conditions; the inlet and outlet pressure, CO_2 and water out flowrate, the irreducible water saturation and endpoint effective and relative permeabilities of CO_2 were measured and analyzed.

In this study, the difference between the pressure transducer readings at the inlet and outlet sides of the core sample has been used to calculate the differential pressure. The differential pressure during horizontal CO_2 injection is largely influenced by the capillary and viscous forces. The capillary forces are controlled mainly by the CO_2-water interfacial tension, contact angle (i.e. wetting status), pore diameter and geometry (Alkan et al., 2010; Bikkina et al., 2016; Chatzis and Morrow, 1984; Fulcher Jr et al., 1985). The wetting status plays an important role in determining the imbibition and the distribution of the wetting and non-wetting phases inside the porous media (Chalbaud et al., 2007; Espinoza and

Santamarina, 2010). The capillary forces, which are responsible for the entrapment of one phase by another during immiscible displacements in porous media (Akbarabadi and Piri, 2013; Chatzis and Morrow, 1984), arise from the presence of the interface between the immiscible fluids (Bikkina et al., 2016) and significantly dominate the multiphase flow, especially in low permeability rocks and fractured reservoirs (Schembre and Kovscek, 2003). On the other hand, the viscous forces are controlled mainly by the viscosity of both displacing and displaced fluids, the fluid velocity in the pores, the amount of each fluid (i.e. saturation) in the pore, and the core sample properties (e.g. frontal area, permeability, and length). Espinoza and Santamarina (Espinoza and Santamarina, 2010) proposed the following equation to account for the impact of the capillary and viscous forces on the differential pressure as follow:

$$\Delta P = P_{CO2} - P_{water} = 4\,\frac{\sigma_{CO_2-water}\,COS\theta}{d} + v\,\frac{32\,L}{d^2}\left(\frac{l_{CO_2}\mu_{CO_2}+l_{water}\mu_{water}}{L}\right) \quad (1)$$

Where ΔP is the differential pressure across the core sample (Pa). P_{CO2} and P_{water} are the pressures of CO_2 phase and water phase, respectively. $\sigma_{CO2\text{-}water}$ is the CO_2-water interfacial tension (mN/m), θ the contact angle, d (m) the diameter of the largest effective pore (Chiquet et al.; Chiquet et al., 2007; Farokhpoor et al., 2013b; Han et al., 2010), L (m) the length of the core sample, l (m) the length of CO_2 or water phase inside the core sample, v (m/s) the fluid velocity in the pores, and μ (Pa·s) the viscosity of the fluids. The first term of Eq.1 refers to the Young-Laplace equation, which accounts for the capillary forces, while the second term refers to the Poiseuille's equation (Espinoza and Santamarina, 2010; Li, 2015), which account for the viscous forces. For small injection rate and high viscosity contrast conditions the impact of viscous forces can be neglected, thus Eq.1 can be reduced to the Young-Laplace equation (Li, 2015) as follows:

$$\Delta P = P_{CO2} - P_{water} = 4\,\frac{\sigma_{CO_2-water}\,COS\theta}{d} \quad (2)$$

The Young-Laplace equation is used to determine the critical pressure point, which is the differential pressure required for the displacing fluid to enter the core sample for the first time. The

non-wetting fluid cannot enter the core sample unless its pressure becomes higher than the critical pressure point (Han et al., 2010).

In this study, the experimental results have been categorized into two main sections. The first section presents and discusses the impact of the experimental fluid pressure, temperature and CO_2 injection rate on the differential pressure profiles while the second section deals with the impact of the parameters investigated on the endpoint CO_2 effective (relative) permeability and irreducible water saturation.

It should be noted that during this study, the term low and high-fluid pressure refers to the experiments conducted at pressures less and higher than 50 bar, respectively. The low and high temperature refers to the experiments performed at less or higher than 33 °C, respectively. The low, medium and high injection rates refer to the experiments performed at injection rate ranging from 0.1 to 0.2 ml/min, from 0.3 to 0.6 ml/min, and from 1 to 2 ml/min, in sequence. The corresponding time refers to the time required to reach the maximum-differential pressure at the start of the experiment. The quasi-differential pressure refers to the differential pressure at the end of the experiment.

3.1 Differential Pressure Profile of GCO_2-Water Drainage Displacements

To investigate the effect of fluid pressure, experimental temperature, and CO_2 injection rate on the differential pressures, series of GCO_2-water displacements were performed at various fluid pressures (from 40 to 70 bar), experimental temperatures (29-45 °C) and CO_2 injection rates (0.1-2 ml/min).

3.1.1 Effect of Fluid Pressure on the Differential Pressure Profile of GCO_2-Water Drainage Displacements

Figure 2 presents the impact of increasing fluid pressure on the differential pressure profile of GCO_2-water drainage displacements. A number of trends are identifiable: Firstly, the differential pressure profile at all fluid pressures is characterized by a high initial increase, immediately followed by a steep rapid reduction and then followed by a quasi-differential pressure. Secondly, there are

multiple oscillations of these cycles. The frequency of these oscillating cycles increases as fluid pressure increases along with a rise in the values of the maximum and quasi-differential pressures.

The high initial increase in the differential pressure can be related to the capillary pressure. The following reduction in the differential pressure profile reflects the impact of the reduction in both capillary forces and viscous forces according to Eq.1. The injection of gaseous CO_2 into the core sample generates the initial increase in differential pressure to overcome the capillary entry pressure for the invasion of the gaseous CO_2 (Chang et al., 2013). The reduction in the capillary forces can be associated with the reduction in the pore resistance to CO_2-water interfaces as the number of pores opened by CO_2 is increased (Kwelle, 2017). This agrees very well with Kwell's finding, who noticed a high reduction in the differential pressure profile as the CO_2-water interface is displaced out of microcapillary tubes (Kwelle, 2017). The reduction in the viscous forces can be related to the combined effect of the dynamic change in relative permeability of gaseous CO_2 and water and the high rate replacement of a more viscous fluid (water) with a less viscous fluid (CO_2) (Chang et al., 2013). Replacing water by CO_2 at a high rate can be linked to (a) the high mobility ratio due to the high viscosity contrast and (b) gas expansion effects which generate an increase in volumetric CO_2 injection rate inside the core sample.

- The gas expansion can, in turn, be related to the density change of the injected CO_2 due to the temperature difference between inside the water bath (i.e. 29 to 45 °C depending on the experimental conditions) and outside it (room temperature 18-20 °C). The density of the injected CO_2 varies as the CO_2 enters the water bath dependant on the injection rate, fluid pressure and the temperature difference from the pump to the sample. The density ratio (d_r) suggested by Perrin and Benson (Perrin and Benson, 2010) has been used to calculate the injection rate inside the core sample. For instance, at an experimental pressure of 40 bar, an injection rate of 1 cm^3/min at 20 °C becomes 1.7522 cm^3/min at 33 °C. However, at an experimental pressure of 70 bar and the same injection rate and temperature conditions, it becomes 5.281cm^3/min.

$$d_r = \frac{P1\,T_2 Z_2}{P2\,T_1 Z_1} \quad (3)$$

Figure 2 reveals that the differential pressure profiles are characterized by multiple differential pressure (PD) oscillations. The appearance of these PD oscillations can be related to the impact of the capillary forces at the trailing end of each CO_2-water slug during CO_2 flooding (Nutt, 1982) or the capillary end effects. According to Nutt, the impact of the capillary forces at the trailing end of the CO_2-water slug is governed by the wetting status of the injected fluid. If a non-wetting fluid (e.g. CO_2) is injected, then the capillary forces will work in an opposite direction to the applied viscous forces. Thus, as water depletion is progressed, the applied viscous forces will drop until they become less than the capillary forces. Upon reaching this point, the flow of the non-depleted capillaries is potentially blocked by the capillary forces (Nutt, 1982). This blockage occurs due to a re-imbibition process of the wetting phase inside the core sample, which was noticed by Hildenbrand et al (Hildenbrand et al., 2002). Hildenbrand et al. observed that the re-imbibition process occurs when the excess pressure in the non-wetting phase declines after the gas breakthrough (Hildenbrand et al., 2002), as shown in Figure 3. This re-imbibition process occurs in a progressive manner starting with the smallest pores and continuing to the larger pores, leading to the successive loss of the interconnected flow-paths, which, in turn, leads to a progressive decline in the non-wetting phase relative permeability. Finally, when the last interconnected flow-path for the non-wetting phase is blocked, the permeability of the non-wetting phase will drop to zero (Hildenbrand et al., 2002). According to Hildenbrand et al., this re-imbition process can result in a residual water saturation when certain-gas filled pores become isolated a result of interrupting the flow pathways. The maximum differential pressure required to open the flow paths again can be used to determine the largest effective pore radius and, hence, the sealing efficiency of the rock (Hildenbrand et al., 2002).

Therefore, since our core sample is water-wet, the pressure of the injected CO_2 had to build up to a certain level to overcome the capillary forces that blocked the CO_2 outflow rate (Nutt, 1982). Due to the high compressibility nature of the gaseous CO_2, the injected CO_2 will accumulate inside the core

sample and the connections pipes until the differential pressure becomes high enough to overcome the capillary forces. Once the blocked capillaries are opened to flow, the cumulative CO_2 will expel the liquid drops that block the pores out of the core sample quickly; the rate of expulsion is expected to increase with the fluid pressure. The development of this phenomenon is highly influenced by the core sample properties and the injection rate due to their direct impact on viscous and capillary forces. As a result, this phenomenon is expected to be reduced when the injection rate, i.e. viscous pressure drop, becomes high enough to overcome the capillary forces (Nutt, 1982). However, due to the cyclic reduction of the viscous pressure drop (i.e. viscous forces) to the level that becomes insufficient to overcome the capillary forces, this phenomenon of oscillations can occur frequently.

On the other hand, since the GCO_2-water displacements are strongly influenced by the capillary end effects and viscous instabilities (Müller, 2011), it might be suggested that the appearance of the oscillations is due to the impact of capillary end effects. The capillary end effects occur at both inlet and outlet faces of the core sample, but its impact becomes more severe at the outlet face. According to Müller, the capillary end effects can never be entirely prevented but can be corrected for (Müller, 2011). The impact of capillary end effects and viscous instabilities can be reduced when the following scaling coefficient proposed by Rapoport and Leas for stabilized floods becomes greater than one.

$$Lu\mu \geq 1 \quad (4)$$

where L is the length of the medium (cm), u the Darcy velocity (cm/min), and μ the displacing phase viscosity (cp) (Fathollahi and Rostami, 2015). The scaling coefficients for the 40, 50, and 70 bar displacements are 0.0773, 0.0844, and 0.285, respectively. The scaling coefficients increased significantly as the fluid pressure increased from 40 and 50 bar to 70 bar, which indicates a reduction in the impact of capillary end effects with increasing fluid pressure. However, since the data from Figure 2 reveal an increase in the frequency of the oscillations with increasing fluid pressure, this indicates that the capillary end effects are not responsible for the PD oscillation phenomenon. In addition, the

disappearance of the oscillations at lower injection rates as shown in Figure 7 further supports the idea that the oscillations are not because of the capillary end effects.

Figure 2 also shows that increasing fluid pressure leads to an increase in the rate of the differential pressure (PD) oscillations along with increases in the values of the maximum and quasi-differential pressures and a reduction in the corresponding time (the time required to reach the maximum-differential pressure at the start of the experiment). For illustration, it can be seen that as the fluid pressure increased from 40 to 50 bar, the rate of the PD oscillations increased by around 33% and the maximum-differential pressure increased by about 2.50%. The quasi-differential pressure was constant at around 1 bar. The corresponding time declined by approximately 17%. However, as the fluid pressure increased from 50 to 70 bar, the PD oscillations substantially increased by 225%, the maximum-differential pressure raised by around 9% and the quasi-differential pressure increased by 165%. The corresponding time dropped considerably by around 78%. The high reduction in the corresponding time with increasing fluid pressure can be related mainly to the increase in gaseous CO_2 density and the injection rate inside the core sample due to the expansion effects. As gaseous CO_2 becomes denser, it requires lesser time to be compressed to the required pressure.

The increase in the maximum and quasi-differential pressures with increasing fluid pressure can be related mainly to the magnitudes of both viscous and capillary forces. According to Eq.1, as the fluid pressure increases the viscous forces increase [due to the increase in CO_2 viscosity and the injection rate inside the core sample due to expansion impact], while the capillary forces decrease [because of the reduction in the CO_2-water interfacial tension (IFT) (Georgiadis et al., 2010) and the increase in the contact angle (Banerjee et al., 2013) due to increasing CO_2 solubility (Bennion and Bachu; Yang et al., 2007)]. Thus, the increase observed in the differential pressures is the net result of the increase in the viscous forces and the reduction in the capillary forces. Reducing capillary forces with increasing pressure is expected to cause a reduction in the extent of differential pressure increase.

The increase in the PD oscillations means the frequency of liquid drops expelled out of the core sample is increased. This can be associated mainly with the reduction in the capillary forces and the increase in gas density with increasing pressure. Increasing the gas density and reducing capillary forces mean less time was required to reach a differential pressure value which was sufficient to overcome the capillary forces; thus, increasing the frequency of the PD oscillations.

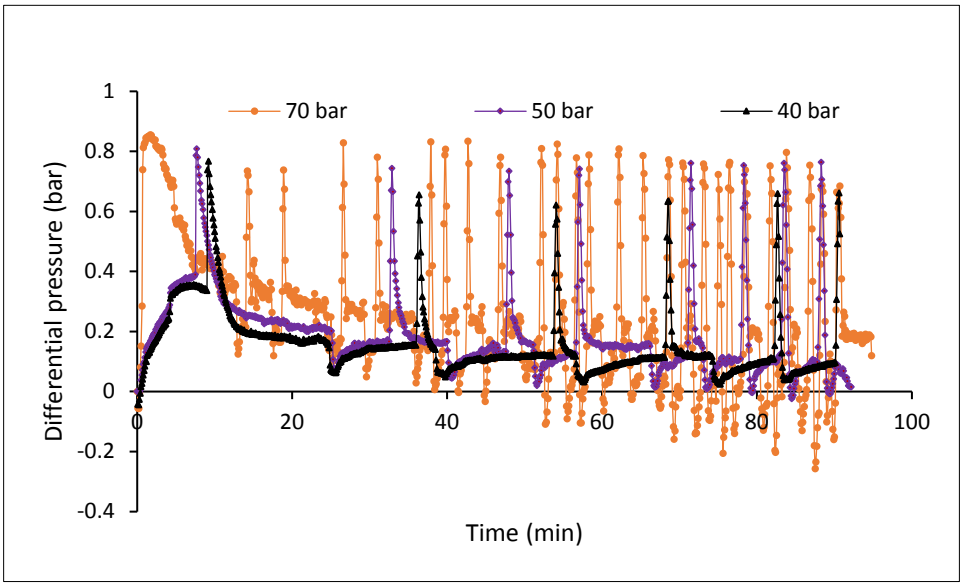

Figure 2: Effect of fluid pressure on the differential pressure profile of GCO_2-water displacements conducted at 0.4 ml/min and 33 °C.

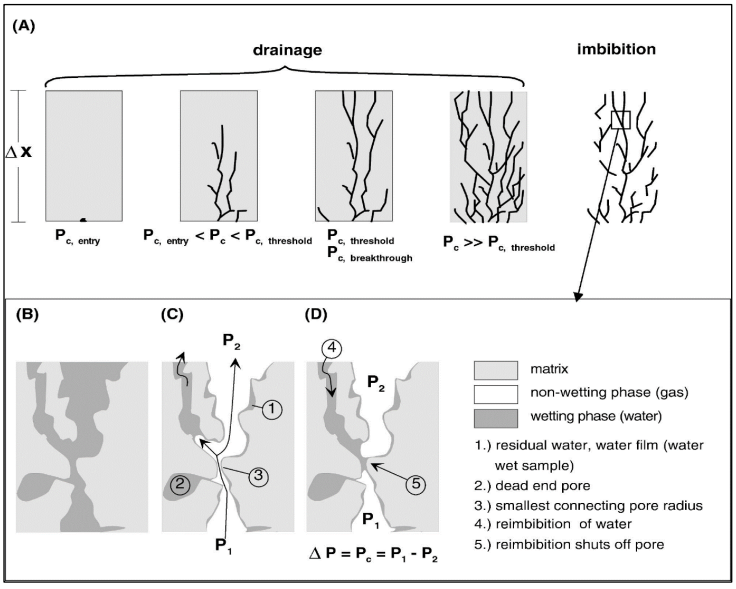

Figure 3: Re-imbibition process in fine-grained rocks (schematic re-imbibition); (A) drainage, (B) initially water-saturated sample, (C) gas breakthrough, (D) re-imbibition (Hildenbrand et al., 2002).

3.1.2 *Effect of Temperature on the Differential Pressure Profile of GCO$_2$-Water Displacements*

Figure 4 presents the impact of increasing experimental temperature on the differential pressure profile. The results demonstrate that the increase in the experimental temperature has a significant impact on the differential pressure profile. Firstly, increasing the temperature increases the frequency of the PD oscillations. At an experimental temperature of 29 °C, the differential pressure profile experienced no oscillations. However, as the temperature increased to 31 °C, the oscillations appeared for the first time. A further increase in the temperature to 33 °C caused the number of oscillations to increase by double. Secondly, the increase in the temperature prompts an increase in the magnitude of the maximum-differential pressure. The quasi-differential pressure was almost constant due to the slight impact of both capillary forces and viscous forces at the end of core flooding.

The appearance and frequency of the PD cycles with increasing temperature have three potential explanations. The first potential reason behind the onset of the oscillations and their frequency is the increase in the capillary forces despite the slight increase in viscous forces under these conditions. The increase in temperature leads to an increase in the CO_2-water IFT (Iglauer et al., 2012) with a reduction in the contact angle (Yang et al., 2007) due to the decline in the CO_2 solubility (Bennion and Bachu; Yang et al., 2007) as well as a slight increase in CO_2 viscosity, and a slight increase in CO_2 injection rate inside the core sample due to expansion effect. For illustration, as the experimental temperature increased from 29 to 31 °C, CO_2-water IFT increases from to 42.9 to 44.42 mN/m, CO_2 viscosity increases very slightly from 16.72 to 16.755 × [10^{-6}(Pa·s)] and CO_2 injection inside the core sample increased from around 0.45 to 0.46 ml/min. However, a further increase in the experimental temperature to 33 °C caused the CO_2-water IFT to decrease to 34.1 mN/m (Bachu and Bennion, 2008a), CO_2 viscosity to increase to 16.805 × [10^{-6}(Pa·s)] and CO_2 injection to increase to 0.466 ml/min.

The second possible reason might be related to the fluctuating behaviour in the CO_2-water IFT when the experimental temperature is around the critical point (Bennion and Bachu), as shown in Figure 5. The third potential reason is that the PD oscillations might occur because of increasing

334 temperature which results in a quicker increase in the movement of CO_2 molecules. This is because each
335 individual molecule has more energy as it becomes hotter, according to the Kinetic molecular theory
336 (Physics, 2017). A high energetic CO_2 molecule might open the closed flow path, due to the increase in
337 capillary forces, quicker.

338 The results indicate that for the sandstone core sample (from the Guillemot A field, North Sea)
339 used in the experiment and under the aforementioned experimental conditions, the onset temperature
340 point of the oscillations is around 31 °C. The characteristics of the sandstone sample, e.g. pore size
341 distribution, play a key role in the onset of the PD oscillations phenomena as they have a direct
342 influence on the magnitude of the capillary forces as illustrated by Young-Laplace law (Eq.2).

343 The data also reveals that as the experimental temperature increased from 29 to 31 °C, the
344 maximum-differential pressure increased by around 12.5% (from 0.72 to 0.81 bar) and the
345 corresponding time dropped by around 9.1% (from 12.1 to 11 min). However, increasing the
346 temperature from 31 to 33 °C caused the differential pressure to decline slightly by 1.23% (from 0.82 to
347 0.81 bar) and the corresponding time dropped by 30% (from 11 to 7.7 min). The increase and decrease
348 in the maximum-differential pressure can be related mainly to the increase or decrease in the capillary
349 forces due to CO_2-water IFT, as stated above. The highest reduction in the corresponding time occurred
350 as the temperature increased to 33 °C. This can be related to the highest reduction in the CO_2-water IFT
351 (Bennion and Bachu), as shown in Figure 5.

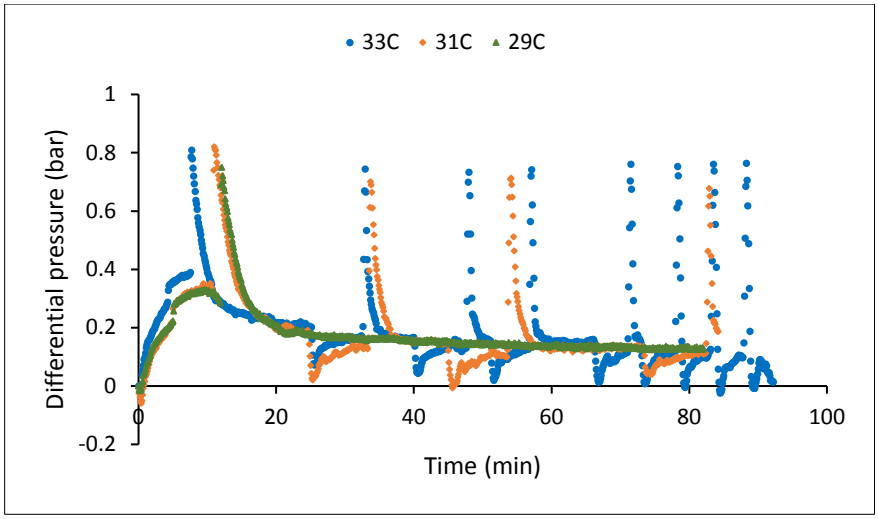

352

353 Figure 4: Effect of temperature on the differential pressure profile of GCO_2-water displacements
354 conducted at 50 bar and 0.4 ml/min.

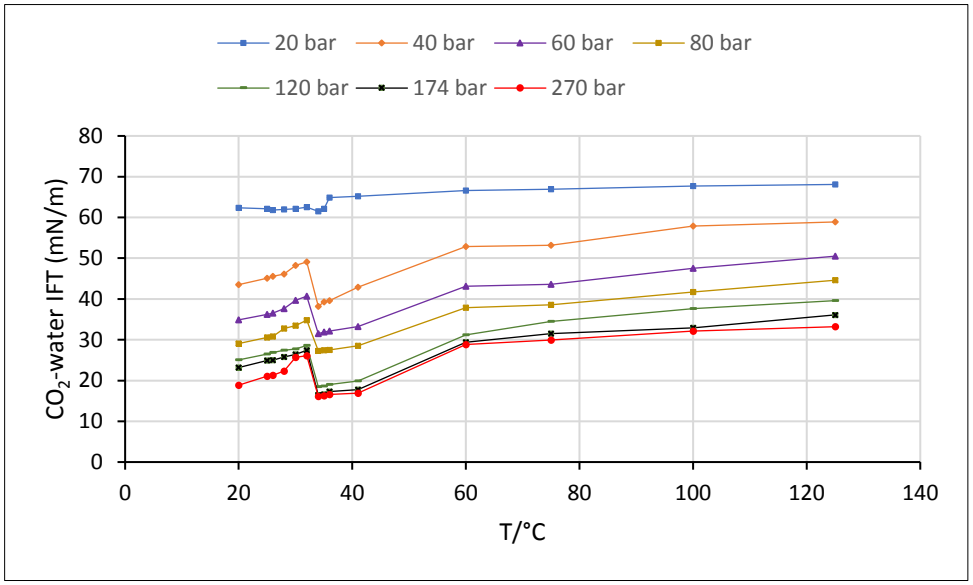

355

356 Figure 5: Interfacial tension for CO_2-Pure Water Systems adopted from (*Bachu and Bennion, 2008b*).

357 To further investigate the effect of the temperature on the differential pressure profile, and
358 especially on the PD oscillations, additional GCO_2-water displacement experiments were conducted
359 under a high-pressure of 70 bar and higher temperature conditions.

360 The data from Figure 6 shows that increasing the experimental temperature by 12 degrees (from
361 33 to 45 °C) at a high-pressure caused no further increase in the rate of the PD oscillations. Yet, it
362 instigated a very slight increase in the maximum and quasi-differential pressures with a small reduction
363 in the corresponding time. The maximum differential pressure increased by only 4.2% (from 0.854 to

0.89 bar) and the quasi-differential pressure by 4.81% (from 0.208 to 0.218 bar). The corresponding time declined by around 17% (from 1.8 to 1.5 min).

The data showed no further increase in the PD oscillations occurred when there are no fluctuations in the IFT as the temperature increased from 33 to 45 °C, as shown in Figure 5. This suggests that the IFT fluctuations might have highly influenced the frequency of PD oscillations.

The increase in the maximum and quasi-differential pressures can be related to the increase in the capillary forces (because of the increasing CO_2-water interfacial tension and the reducing contact angle (Yang et al., 2007)), and the slight increase in the viscous forces (because of the increasing injection rate). The magnitude of the viscous forces might have slightly declined because of the slight reduction in CO_2 viscosity with increasing temperature. For illustration, as the experimental temperature increased from 33 to 45 °C, the CO_2-water IFT increases from around 29.15 to around 33.4 mN/m (Bennion and Bachu), and the CO_2 injection rate inside the core sample increased from 1.315 to 1.748 ml/min but the viscosity decreases from 20.743 to 19.05 × [10^{-6}(Pa·s)].

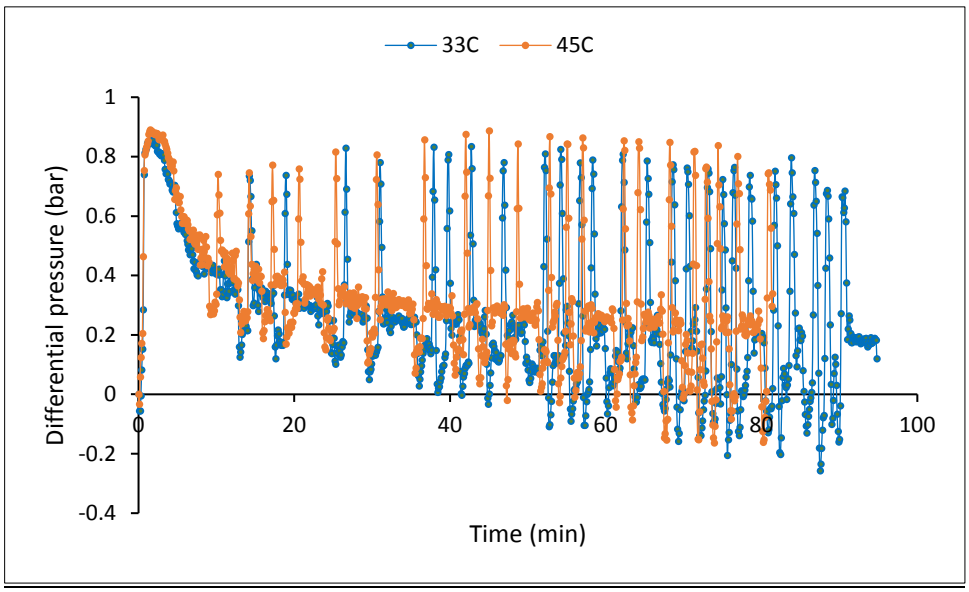

Figure 6: Effect of temperature on the differential pressure profile of GCO_2-water displacements conducted at 70 bar and 0.4 ml/min.

3.1.3 *Effect of CO_2 Injection Rate on the Differential Pressure Profile of GCO_2-Water Core Floodings*

Figure 7, Figure 8 and Figure 9 show the impact of increasing CO_2 injection rate on the differential pressure profile. For Figure 8, the experiments conducted at higher injection rate (2 ml/min) lasted shorter than those conducted at lower injection rate (1 ml/min) to explore the impact of injection volumes on the displacement efficiency. The results reveal that increasing the injection rate has a significant impact on the differential pressure profile, mainly at early stages of core flooding. The data reveal a number of important observations (**A-E**).

A) The data show that the higher the injection rate, the higher the maximum differential pressure is. However, increasing the injection rate caused a slight increase in the quasi-differential pressure; the corresponding time decreased at low injection rates and increased at high injection rates. For illustration, as the CO_2 injection rate increased from 0.1 to 0.2 ml/min, the maximum-differential pressure increased by 33.54% (from 0.161 to 0.215 bar), and the quasi-differential pressure by 5.88% (from 0.068 to 0.072 bar) while the corresponding time reduced by almost half (from 13.5 to 6.5 min). However, as the CO_2 injection rate increased from 1 to 2 ml/min, the maximum-differential pressure increased by around 44% (from 0.833 to 1.201 bar), the quasi-differential pressure increased by around 15% (from 0.254 to 0.291 bar), and the corresponding time increased by 12% (from 3.3 to 3.7 min). The increase in the corresponding time at high injection rates despite the increase in the CO_2 injection rate can be related to the high increase in the magnitude of the maximum-differential pressure as well as the low-density nature of the gaseous CO_2. Since the injected gaseous CO_2 was at low pressure (40 bar), it needed a longer time to reach the higher maximum-differential pressure of 1.201 bar during the 2 ml/min-displacement.

B) The data from Figure 7 and Figure 8 reveals that as the injection rate increased by tenfold (from 0.1 to 1 ml/min, and from 0.2 to 2 ml/min), the quasi-differential pressure increased by only around fourfold, (from 0.068 to 0.254 bar, and from 0.072 to 0.291 bar). This might be related to a potential

405 increase in the relative permeability with increasing injection rate (Akbarabadi and Piri; Chang et al.,
406 2013) that leads to a reduction in the viscous pressure drop.

407 **C**) The data previously shown in Figure 2 reveals that the differential pressure profile of the 40
408 bar-experiments is characterized by PD oscillations at 0.4 ml/min CO_2 injection rate. Surprisingly, the
409 data from Figure 7 and Figure 8 reveal no PD oscillations at lower and higher CO_2 injection rates. The
410 disappearance of the PD oscillations at higher injection rates (e.g. 1-2 ml/min) can be related to the high
411 increase in the pressure drop due to viscous forces. Thus, the viscous forces impeded the capillary
412 forces, which are responsible for the observed PD oscillations phenomenon (Nutt, 1982). On the other
413 hand, at lower CO_2 injection rates (e.g. 0.1 to 0.2 ml/min), CO_2 might flow through preferential inlet and
414 outlet pores (Gunde et al., 2010) that are characterized by low resistance to flow and by less capillary
415 forces. Consequently, CO_2 does not need to pass through the smallest channels that are characterized
416 by higher resistance to CO_2 flow and higher capillary forces, hence avoiding the impact of the capillary
417 forces that cause the oscillations.

418 **D**) To look in detail at the unexpected results regarding the appearance and disappearance of the
419 PD oscillations and the impact of CO_2 injection rate on the differential pressure profile, further
420 experiments were conducted at 40 bar and over a more detailed range of injection rates, as shown in
421 Figure 9. It should be noted that the 0.4 ml/min GCO_2-water displacement is repeated to make sure that
422 the observations were not an experimental error.

423 The results from Figure 9 show clearly that the PD oscillations occurred only at 0.4 ml/min for the
424 experiments conducted at a low pressure of 40 bar. Overall, the data confirm that the increase in the
425 injection rate produces an increase in the maximum-differential pressure and a reduction in its
426 corresponding time for this range of injection rates. The quasi-differential pressure reduced slightly
427 due to the potential increase in the relative permeabilities (Akbarabadi and Piri; Chang et al., 2013).

428 The data from Figure 9 can be divided into two groups. The first group includes the experiments
429 conducted at a CO_2 injection rate of 0.3 and 0.4 ml/min while the second group involves the experiments

performed at 0.5 and 0.6 ml/min. As the CO_2 injection rate increased for the first lower injection rate group, the maximum-differential pressure was almost constant at around 0.76 bar, but the corresponding time reduced by 25% (from around 20 to 15 min). The second higher injection rate group is characterized by a constant maximum-differential pressure of 0.938 bar and a constant corresponding time of 6.5 min. Thus, the data reveals that shifting the CO_2 injection rate to the second group caused the maximum-differential pressure to increase by 23.42% and the corresponding time to reduce by around 57%. The increase in the maximum-differential pressure associated with shifting the CO_2 injection rate might be related to the properties of the core sample. It might have occurred because as the injection rate increased from the first to the second group, the maximum-differential pressure had to further increase to open new preferential flow paths for the injected CO_2 (Gunde et al., 2010). The nearly constant maximum-differential pressure for each group might indicate a minimal impact for the viscous forces on the differential pressure at low pressures. It indicates also that the expected increase in the maximum-differential pressure due to increasing injection rate is reduced by the potential increase in the relative permeability due to the increasing injection rate (Akbarabadi and Piri; Chang et al., 2013).

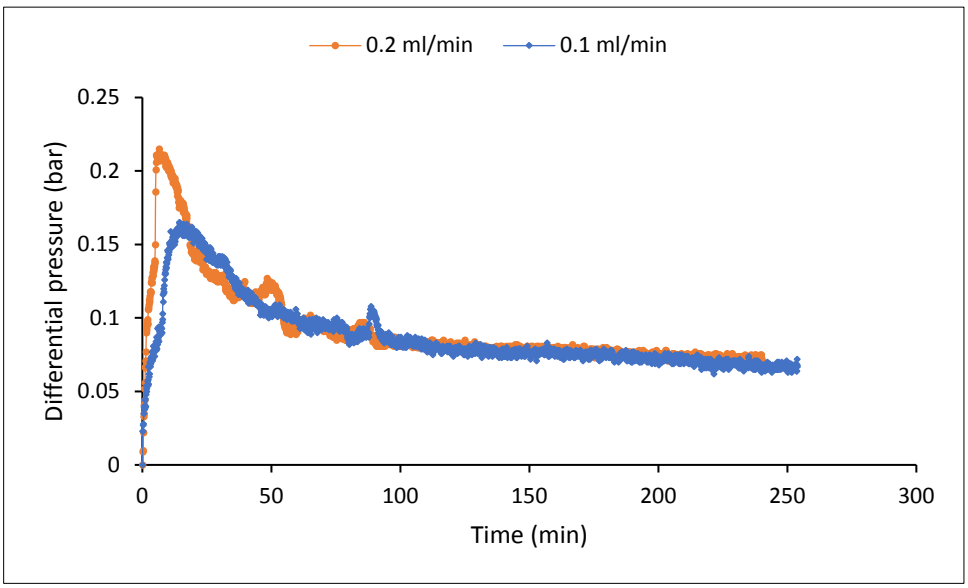

Figure 7: Effect of CO_2 injection rate on the differential pressure profile of GCO_2-water displacements conducted at 40 bar and 33 °C.

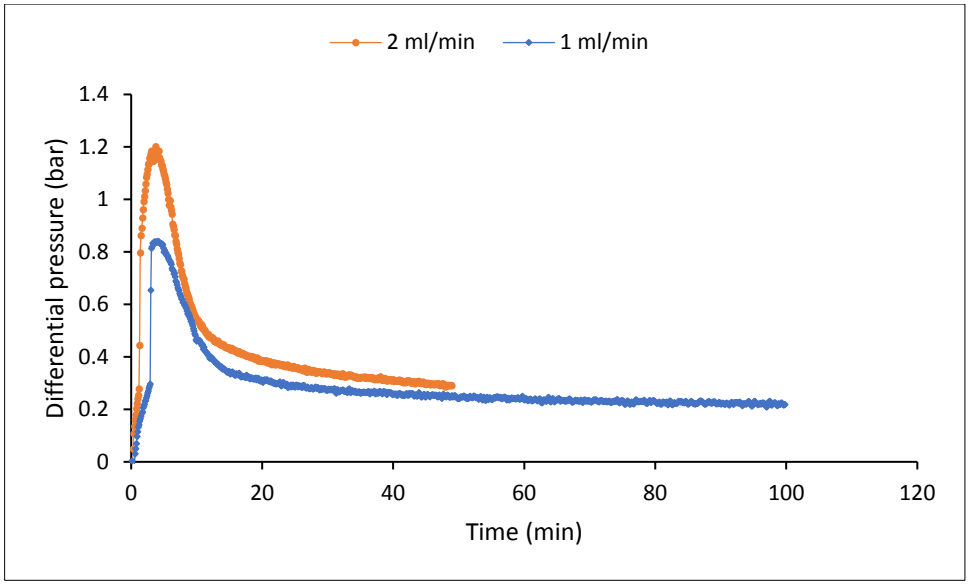

448

449 Figure 8: Effect of CO_2 injection rate on the differential pressure profile of GCO_2-water
450 displacements conducted at 40 bar and 33 °C.

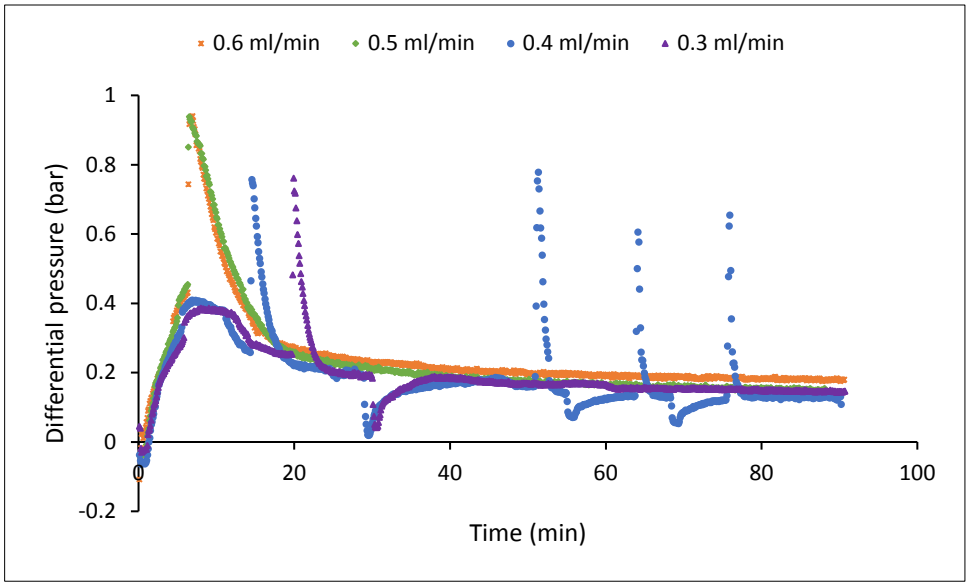

451

452 Figure 9: Effect of CO_2 injection rate on the differential pressure profile of GCO_2-water
453 displacements conducted at 40 bar and 33 °C.

454 **E**) To further investigate the effect of CO_2 injection rate on the differential pressure profile and the
455 phenomenon of the PD oscillations particularly, a second set of GCO_2-water displacements have been
456 performed at a higher pressure (70 bar). To enable a clear comparison, the data was presented in two
457 figures: Figure 10 and Figure 11.

458 **E.1**) The data shows clearly that conducting GCO_2-water displacements at higher pressure (70 bar)
459 caused the PD oscillations to appear over a wider range of CO_2 injection rates (from 0.2 to 1 ml/min). It
460 reveals also that the change in the maximum and quasi-differential pressures, corresponding time and
461 PD oscillations depend on the range of the injection rate; the highest change occurred as the injection
462 rate increased from 0.4 to 1 ml/min. For illustration, as the CO_2 injection rate increased from 0.4 to 1
463 ml/min, the maximum-differential pressure increased considerably by around 258% (from 0.845 to
464 3.024 bar) and the quasi-differential pressure increased by around 224.5% (from 0.265 to 0.86 bar). The
465 corresponding time prolonged by 140% (from 1 to 2.4 min), despite the increase in the injection rate,
466 due to the increase in the maximum-differential pressure. The frequency of the PD oscillations was
467 almost constant for the last 20 min of both experiments. The increase in the maximum and quasi-
468 differential pressures can be attributed to the increase in the viscous forces; the increase in the
469 corresponding time can be related to the high increase in the magnitude of the maximum differential
470 pressure.
471 **E.2**) On the other hand, as the CO_2 injection rate increased from 0.2 to 0.4 ml/min, the maximum-
472 differential pressure was almost constant at around 0.85 bar, the quasi-differential pressure slightly
473 increased, the corresponding time slightly reduced, and the frequency of the PD oscillations
474 considerably decreased but the magnitude of the PD oscillations significantly increased from around
475 0.25 to 0.825 bar. The nearly constant maximum-differential pressure (0.85 bar) at the low injection rates
476 (0.2 to 0.4 ml/min)-core floodings reveals a negligible impact of the viscous forces on the differential
477 pressure at the conditions investigated. However, the reduction in the frequency of the PD oscillations
478 might be attributed to CO_2 flow through preferential flow paths (Gunde et al., 2010).
479 The frequency of the PD oscillations might depend to a considerable extent on the core sample
480 properties, the change in CO_2 distribution due to the change in the CO_2 injection rate, and the
481 operational conditions. For illustration, as the CO_2 injection rate increased from 0.2 to 0.4 ml/min, the
482 CO_2 might have distributed over a wider range of capillaries. Consequently, as the viscous pressure
483 drop declined because of water depletion, the CO_2 flow inside the smaller capillaries was blocked due

484 to their higher resistance to CO_2 flow. Later, as the pressure drop continued, the CO_2 flow in larger
485 capillaries was blocked, too. Ultimately, it came to the point when all capillaries were blocked by the
486 capillary forces (Hildenbrand et al., 2002; Nutt, 1982). Thus, the increase in CO_2 distribution with
487 increasing injection rate might have led to prolonging the time required for the capillary forces to block
488 the CO_2 production from all opened interconnected flow paths. As a result, since the volume of the
489 opened capillaries were larger with increasing injection rate from 0.2 to 0.4 ml/min; therefore, the
490 frequency of the PD oscillations was reduced.

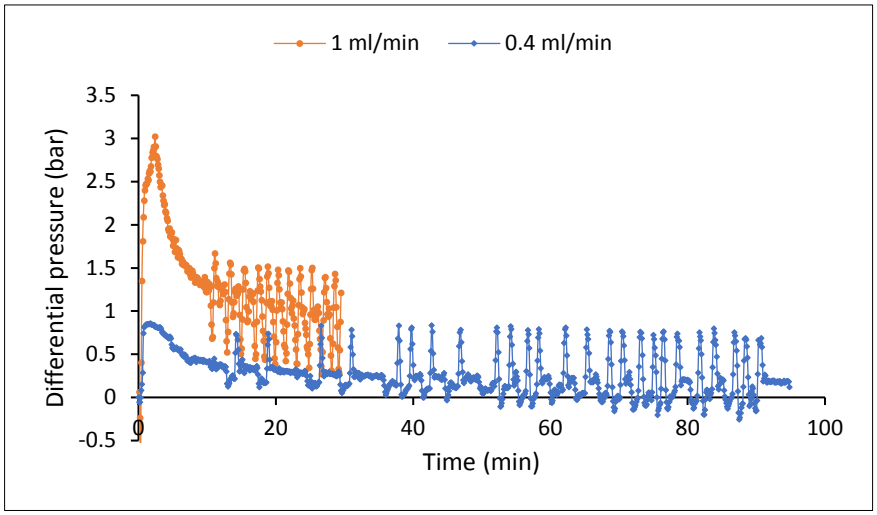

491

492 Figure 10: Effect of CO_2 injection rate on the differential pressure profile of GCO_2-water displacements
493 conducted at 70 bar and 33 °C.

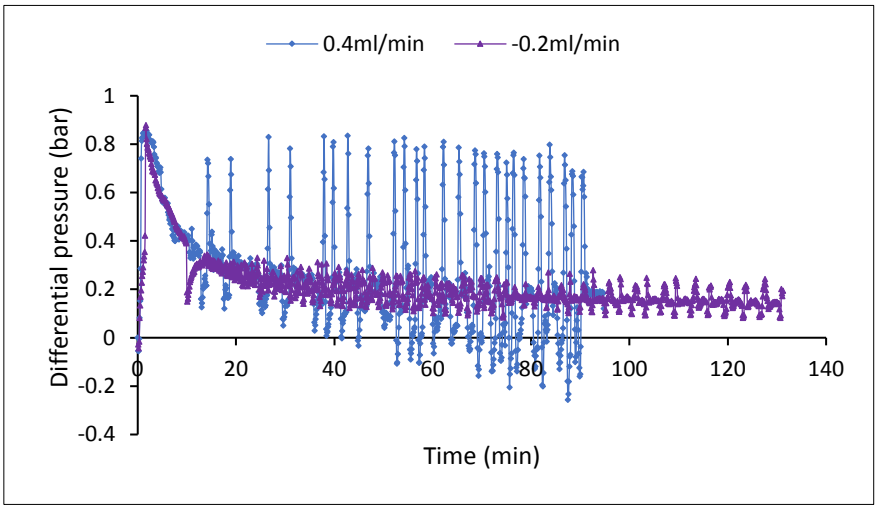

494

495 Figure 11: Effect of CO_2 injection rate on the differential pressure profile of GCO_2-water
496 displacements conducted at 70 bar and 33 °C.

In summary, fluid pressure, temperature and CO_2 injection rate exert significant influences on the differential pressure profile of the GCO_2-water drainage displacements. The differential pressure profile at all fluid pressures, temperatures and injection rates is characterized by a high initial increase immediately followed by a steep rapid pressure reduction and then by a quasi-pressure drop.

The differential pressure is controlled by the interplay of both capillary and viscous forces. The increase in capillary forces leads to the appearance of the PD oscillations (the onset points) while the increase in viscous forces causes their impedance.

There are multiple cycles of these oscillations and the occurrence and frequency of these oscillations vary with fluid pressure, temperature and injection rate. The frequency of these oscillating cycles increases as fluid pressure and fluid temperature increase but vary with injection rate and seem to be fluid pressure dependent. These oscillations occurred only at 0.4 ml/min at low pressures (i.e. 40 bar), but they appeared over a wider range of injection rates at higher pressures (i.e. 70 bar). The maximum-differential pressure reached during each cycle increases with increasing fluid pressure, temperature and injection rate.

3.2 *Effect of Fluid Pressure, Temperature, and Injection Rate on Irreducible Water Saturation and Endpoint Effective and Relative Permeabilities of CO_2*

The effective and relative permeabilities of CO_2 are significantly important to the determination of the efficiency and integrity of CO_2 sequestration in subsurface formations (Busch and Müller, 2011; Rathnaweera et al., 2015). At the end of the flooding experiment, the volume of the water produced was measured, and the irreducible water saturation was calculated. Then, the core sample was weighed to confirm the irreducible water saturation calculations. To calculate the endpoint effective (relative) CO_2 permeability using Darcy's law, the average quasi-differential pressure and the average CO_2 outflow rate of the last period were used (Akbarabadi and Piri; Chang et al., 2013). The CO_2 viscosity at the experimental pressure and temperature was calculated using the Peace software website (Peace software, 2017).

The results from Table 1 shows that both endpoint CO_2 relative permeability (K_{rCO2}^{max}) (Armstrong et al., 2017) and irreducible water saturation (S_{wr}) are dependent on the experimental conditions at which they are measured. The S_{wr} was in the range of around 0.38-0.45 while the K_{rCO2}^{max} was less than 0.25. Busch and Müller obtained a low relative permeability for CO_2, too (Busch and Müller, 2011). Such

low relative permeability would tend to decrease injectivity while increasing displacements efficiency (Levine et al., 2011).

The results from Table 1 reveal that in general the increase in fluid pressure, temperature, and injection rate lead to an increase in the K_{rCO2}^{max} and a decline in the S_{wr}. In case of increasing fluid pressure and temperature, the high increase in the K_{rCO2} can be attributed mainly to the high increase in the injection rate inside the core sample due to the high impact of gas expansion (Rostami et al., 2010; Skauge et al.). This increase in volumetric CO_2 injection rate might result in forcing the CO_2 to flow through a wider range of the core sample pores.

The displacements efficiency is controlled by many factors that include relative permeability, wetting conditions, viscous fingering, gravity segregation, channelling, the amount of crossflow/mass transfer (Chukwudeme and Hamouda, 2009), mobility ratio, and capillary number (Kazemifar et al., 2015). The capillary number (*Ca*) refers to the ratio of the viscous forces to capillary forces (Lenormand et al., 1988). The mobility ratio (*M*) refers to the ratio of the displaced to the displacing phase viscosities. Increasing the contrast between the viscosity of the displacing and displaced fluid leads to a higher *M* which will result in a more unstable configuration front. The following formulas are used to define them:

$$Ca = \frac{\mu_2 V_2}{\sigma \cos \theta} \quad (5)$$

$$M = \frac{\mu_2}{\mu_1} \quad (6)$$

where μ is the dynamic viscosity, σ the interfacial tension between the displaced and the displacing phases, *1* the subscript of the displaced phase, *2* the subscript of the displacing phase, θ the contact angle between the two fluids and the surface, and V_2 the bulk velocity of the displacing fluid. The flowing equation is used to define the bulk velocity.

$$V_{bulk} = \frac{Q}{A \emptyset} \quad (7)$$

where Q is the volumetric injection rate, A the area of the frontal face of the core sample, and ϕ the core sample porosity (Kazemifar et al., 2015). Based on the magnitudes of the Ca and the M, three different regimes can be defined (Kazemifar et al., 2015). For the GCO_2-water displacement investigated both Ca and M are small, which suggest a capillary fingering regime.

The reduction observed in the S_{wr} can be attributed mainly to the increase in the Ca and the reduction in the M. This is because the Ca and M are the most influential dimensionless parameters that govern GCO_2-water core flooding displacement (Kazemifar et al., 2015). As the Ca increases, the impact of the capillary forces compared to viscous forces decreases. The balance between the viscous forces and capillary forces governs the pore scale drainage displacements (Heaviside and Black, 1983). The capillary forces are responsible for the trapping of the injected CO_2 (Akbarabadi and Piri, 2013; Bachu and Shaw, 2003). Thus, decreasing the capillary forces (e.g. due to the reduction in the interfacial tension) will lower the S_{wr} (i.e. enhance the fluid displacements) (Ahmadi et al., 2015). On the other hand, reducing M will result in a more uniform displacement of water by CO_2 (Bennion and Bachu, 2006), which can result in reducing the S_{wr}. The data from Table 1 show that the increase in the Ca and the reduction in the M can lead to a reduction in the S_{wr} even when the change in both Ca and M is small. Ding and Kantzas observed that the critical Ca for the gas-water system is 2E-8 (Ding and Kantzas, 2007).

The results from Table 1 reveal that increasing the fluid pressure from 40 to 70 bar at 33 °C and 0.4 ml/min caused the $K_{rCO_2}^{max}$ to increase by around 0.099 and the S_{wr} to decrease by around 0.047. The largest increase in the $K_{rCO_2}^{max}$ and the highest reduction in the S_{wr} occurred as the fluid pressure increased from low-fluid pressure displacements (40 and 50 bar) to high-fluid pressure displacements (70 bar). The observed trend of the $K_{rCO_2}^{max}$ and S_{wr} are in agreement with the findings of Liu et al. and Bennion and Bachu (Bennion and Bachu, 2006; Liu et al.). Liu et al also observed an increase in the K_{rCO_2} with increasing pressure (Liu et al.). Bennion and Bachu observed an increase in the K_{rCO_2} and increase in the maximum endpoint CO_2 saturation (i.e. decrease in S_{wr}) with increasing pressure; they attributed

574 that to the reduction in IFT with increasing pressure (Bennion and Bachu, 2006). The observed trend of
575 the $K_{rCO_2}^{max}$ and S_{wr} can also be associated with the relatively high increase in the *Ca* and the high
576 reduction in the *M*.

577 The results from Table 1 reveal that increasing temperature led to an increase in the $K_{rCO_2}^{max}$. On
578 the other hand, increasing temperature caused a reduction in the S_{wr} for the displacements conducted
579 at high-fluid pressure (70 bar) and over a high temperature increase (33-45 °C). Nonetheless, for the
580 experiments conducted at low-fluid pressure (50 bar) and over a small temperature increase (29-33 °C),
581 the trend of the S_{wr} depends on the magnitude of the experimental temperature. For the high-fluid
582 pressure displacements, when the temperature increased from 33 to 45 °C at 70 bar, the $K_{rCO_2}^{max}$
583 increased by around 0.035 and the S_{wr} decreased by around 0.02. The reduction in the S_{wr} for the 70 bar
584 displacements can be attributed also to the high increase in the *Ca* and the high reduction in the *M*. For
585 the low-fluid pressure displacements, as the temperature increased slightly from 29 to 33 °C at 50 bar,
586 the $K_{rCO_2}^{max}$ increased by around 0.016. Nevertheless, the S_{wr} value was between around 0.40 and 0.41.
587 The S_{wr} saturation slightly increased by around 0.01 as the temperature increased from 29 to 31 °C, and
588 then slightly decreased by about 0.005 as the temperature increased from 31 to 33 °C. The slight increase
589 in the S_{wr} might be related to the slight reduction in the *Ca* as well as the impact of the capillary forces,
590 which can be seen through the appearance of the PD oscillations when the temperature increased to 31
591 °C, see Section 3.2 for more information; the PD oscillations might result in hindering water production
592 to a slight extent. On the other hand, the slight reduction in the S_{wr}, when the temperature further
593 increased to 33 °C, can be associated with the relatively high increase in the *Ca* as well as the slight
594 reduction in the *M*.

595 Overall, the results from Table 1 shows that the increase in the CO_2 injection rate caused an increase
596 in the $K_{rCO_2}^{max}$ and a reduction in the S_{wr}. Increasing the injection rate from 0.1 to 2 ml/min at 40 bar and
597 33 °C resulted in an increase in the $K_{rCO_2}^{max}$ by around 0.157 and a reduction in the S_{wr} by around 0.05.
598 These findings agree with those in Chang et al. and Akbarabadi and Piri (Akbarabadi and Piri; Chang

et al., 2013). However, for the core flooding at 0.4 ml/min or less, the S_{wr} trend is not clear. Moreover, the K_{rCO2}^{max} of the experiments conducted at 40 bar-0.2 ml-33 °C does not fit linearly in the trend. Increasing the injection rate from 0.6 to 1 ml/min resulted in the highest reduction in the S_{wr}. This can be corresponded to the high increase in the *Ca* from around 7.9 E-8 to 1.3 E-7. For the core flooding performed at 70 bar and 33 °C, increasing the injection rate from 0.2 to 1 ml/min caused a very slight reduction in the S_{wr} by 0.0077. However, the K_{rCO2}^{max} increased substantially as the injection rate increased from 0.2 to 0.4 ml/min. Nevertheless, as the injection rate increased to 1 ml/min, a significant reduction in the K_{rCO2}^{max} happened again, the reason is not clear. The very slight reduction in the S_{wr} might be because only a slight increase occurred in the *Ca* and that *M* was constant.

Table 1: Effect of fluid pressure, temperature, and injection rate on endpoint effective and relative permeabilities of gaseous CO_2 and irreducible water saturation

Parameter	Experiment	K_{fCO2}	K_{rCO2}	S_{wr}	*M*	*Ca*
Fluid Pressure Effect	40 bar-0.4 ml/min-33 °C	1.768	0.113	0.4244	46.26	5.265E-08
	50 bar-0.4 ml/min-33 °C	1.987	0.127	0.4089	44.56	6.250E-08
	70 bar-0.4 ml/min-33 °C	2.613	0.212	0.3779	36.10	2.504E-07
Temperature Effect	50 bar-0.4 ml/min-29 °C	1.507	0.096	0.4012	48.69	4.748E-08
	50 bar-0.4 ml/min-31 °C	1.738	0.111	0.4147	46.57	4.698E-08
	50 bar-0.4 ml/min-33 °C	1.987	0.127	0.4089	44.56	6.250E-08
	70 bar-0.4 ml/min-33 °C	2.613	0.212	0.3779	36.10	2.547E-07
	70 bar-0.4 ml/min-45 °C	3.675	0.247	0.3566	31.34	2.714E-07
Injection Rate Effect	40 bar-0.1 ml/min-33 °C	0.67	0.043	0.38	46.26	1.316E-08
	40 bar-0.2 ml/min-33 °C	1.265	0.081	0.446	46.26	2.632E-08
	40 bar-0.3 ml/min-33 °C	0.955	0.061	0.436	46.26	3.948E-08
	40 bar-0.4 ml/min-33 °C	1.493	0.095	0.4244	46.26	5.265E-08
	40 bar-0.5 ml/min-33 °C	1.528	0.097	0.436	46.26	6.581E-08
	40 bar-0.6 ml/min-33 °C	1.535	0.098	0.4167	46.26	7.897E-08
	40 bar-1 ml/min-33 °C	1.793	0.114	0.3837	46.26	1.316E-07

40 bar-2 ml/min-33 °C	3.13	0.20	0.391	46.26	2.632E-07
70 bar-0.2 ml/min-33 °C	2.421	0.154	0.3798	36.10	1.273E-07
70 bar-0.4 ml/min-33 °C	3.625	0.167	0.3779	36.10	2.547E-07
70 bar-1 ml/min-33 °C	1.976	0.128	0.3721	36.10	6.368E-07

4. Conclusion

In this paper, the effect of fluid pressure, temperature, and CO_2 injection rate on gaseous CO_2 dynamic behaviour during its flooding of a water-saturated sandstone core sample have been investigated in detail. The results indicate that the parameters investigated have a moderate to significant influence on the differential pressure profile, endpoint CO_2 relative and effective permeabilities and irreducible water saturation.

For all fluid pressures, temperatures, and injection rates, the differential pressure profiles are characterized by a sharp increase, immediately followed by a steep pressure reduction, and finally, by a gradual pressure reduction. The differential pressure profiles are controlled by the interplay of both capillary and viscous forces. The capillary forces produce cyclic oscillations within the differential pressure and fluid production data; the increase in the viscous forces impede the appearance of these oscillations. The appearance and frequency of the oscillations depend on the fluid pressure, temperature, and CO_2 injection rates. In general, the frequency of the oscillations increased with increasing pressure and temperature. The differential pressure oscillation cycles exhibit a very interesting response to varying injection rate, they are dependent on the fluid pressure. At 40 bar, the oscillations were only observed at an injection rate of 0.4 ml/min, whereas at 70 bar the oscillations occurred at all injection rates tested (0.2, 0.4, and 1ml/min).

In general, the increase in fluid pressure, temperature, and injection rate led to an increase in the maximum and quasi-differential pressures; the extent of the increase in the differential pressure is dependent on the fluid pressure, temperature, and injection rate. Increasing the fluid pressure and temperature caused a reduction in the time required to achieve the maximum-differential pressure at

631 the start of the experiment, i.e. corresponding time. Whereas, increasing the injection rate caused the
632 corresponding time to decrease at low injection rates and increase at high injection rates.

633 In general, the increase in fluid pressure, temperature, and injection rate led to an increase in the
634 endpoint CO_2 relative permeability (K_{rCO2}^{max}) and a decline in the irreducible water saturation (S_{wr}). The
635 S_{wr} was in the range of around 0.38-0.45 while the K_{rCO2}^{max} was less than 0.25.

636 **Acknowledgements**: The authors wish to thank the Higher Committee for Education
637 Development in Iraq and the Ministry of Oil in Iraq for their sponsorship of the first author PhD study.

638 # 4 References

639 Aggelopoulos, C., Robin, M., Perfetti, E., Vizika, O., 2010. CO2/CaCl2 solution interfacial tensions under
640 CO2 geological storage conditions: influence of cation valence on interfacial tension. Advances in Water
641 Resources 33, 691-697.
642 Ahmadi, M.A., Hasanvand, M.z., Behbahani, S.S., Nourmohammad, A., Vahidi, A., Amiri, M., Ahmadi,
643 G., 2015. Effect of operational parameters on the performance of carbonated water injection:
644 Experimental and numerical modeling study. The Journal of Supercritical Fluids.
645 Akbarabadi, M., Piri, M., Geologic storage of carbon dioxide: an experimental study of permanent
646 capillary trapping and relative permeability, In Proceedings of International Symposium of the Society
647 of Core Analysts, Austin, Texas, USA. 18–21 September 2011, pp. 18-21.
648 Akbarabadi, M., Piri, M., 2013. Relative permeability hysteresis and capillary trapping characteristics
649 of supercritical CO2/brine systems: An experimental study at reservoir conditions. Advances in Water
650 Resources 52, 190-206.
651 Al-Menhali, A., Krevor, S., 2014. Effective wettability measurements of CO2-brine-sandstone system at
652 different reservoir conditions. Energy Procedia 63, 5420-5426.
653 Al-Zaidi, E., Nash, J., Fan, X., 2018. Effect of CO2 phase on its water displacements in a sandstone core
654 sample. IJGGC 71, 227-238.
655 Alemu, B.L., Aker, E., Soldal, M., Johnsen, Ø., Aagaard, P., 2011. Influence of CO2 on rock physics
656 properties in typical reservoir rock: a CO2 flooding experiment of brine saturated sandstone in a CT-
657 scanner. Energy Procedia 4, 4379-4386.
658 Alkan, H., Cinar, Y., Ülker, E., 2010. Impact of capillary pressure, salinity and in situ conditions on CO2
659 injection into saline aquifers. Transport in porous media 84, 799-819.
660 Armstrong, R.T., McClure, J., Berill, M., Rücker, M., Schlüter, S., Berg, S., 2017. Flow Regimes During
661 Immiscible Displacement. Petrophysics 58, 10-18.
662 Bachu, S., 2000. Sequestration of CO2 in geological media: criteria and approach for site selection in
663 response to climate change. Energy conversion and management 41, 953-970.
664 Bachu, S., 2001. Geological sequestration of anthropogenic carbon dioxide: applicability and current
665 issues. Geological perspectives of global climate change, 285-303.
666 Bachu, S., 2013. Drainage and imbibition CO2/brine relative permeability curves at in situ conditions
667 for sandstone formations in western Canada. Energy Procedia 37, 4428-4436.
668 Bachu, S., Bennion, D.B., 2008a. Interfacial tension between CO2, freshwater, and brine in the range of
669 pressure from (2 to 27) MPa, temperature from (20 to 125)° C, and water salinity from (0 to 334 000) mg·
670 L− 1. Journal of Chemical & Engineering Data 54, 765-775.
671 Bachu, S., Bennion, D.B., 2008b. Interfacial tension between CO2, freshwater, and brine in the range of
672 pressure from (2 to 27) MPa, temperature from (20 to 125)° C, and water salinity from (0 to 334 000) mg·
673 L− 1. Journal of Chemical & Engineering Data 54, 765-775.

674 Bachu, S., Bennion, D.B., 2009. Dependence of CO2-brine interfacial tension on aquifer pressure,
675 temperature and water salinity. Energy Procedia 1, 3157-3164.
676 Bachu, S., Shaw, J., 2003. Evaluation of the CO2 Sequestration Capacity in Alberta's Oil and Gas
677 Reservoirs at Depletion and the Effect of Underlying Aquifers. Journal of Canadian Petroleum
678 Technology 42.
679 Bahralolom, I., Bretz, R., Orr Jr, F., 1988. Experimental investigation of the interaction of phase behavior
680 with microscopic heterogeneity in a CO2 flood. SPE reservoir engineering 3, 662-672.
681 Banerjee, S., Hassenklöver, E., Kleijn, J.M., Cohen Stuart, M.A., Leermakers, F.A., 2013. Interfacial
682 Tension and Wettability in Water–Carbon Dioxide Systems: Experiments and Self-consistent Field
683 Modeling. The Journal of Physical Chemistry B 117, 8524-8535.
684 Basbug, B., Gumrah, F., Oz, B., 2005. Simulating the Effects of Deep Saline Aquifer Properties on
685 COSequestration, Canadian International Petroleum Conference. Petroleum Society of Canada.
686 Bennion, D.B., Bachu, S., The impact of interfacial tension and pore size distribution/capillary pressure
687 character on CO2 relative permeability at reservoir conditions in CO2-brine systems, In Proceedings of
688 the SPE/DOE Symposium on Improved Oil Recovery. Society of Petroleum Engineers: Houston, TX,
689 USA, 2006., Tulsa, OK, USA, 22–26 April 2006.
690 Bennion, D.B., Bachu, S., 2006. Dependence on temperature, pressure, and salinity of the IFT and
691 relative permeability displacement characteristics of CO2 injected in deep saline aquifers, SPE Annual
692 Technical Conference and Exhibition. Society of Petroleum Engineers.
693 Berg, S., Oedai, S., Ott, H., 2013. Displacement and mass transfer between saturated and unsaturated
694 CO2–brine systems in sandstone. IJGGC 12, 478-492.
695 Bikkina, P., Wan, J., Kim, Y., Kneafsey, T.J., Tokunaga, T.K., 2016. Influence of wettability and
696 permeability heterogeneity on miscible CO2 flooding efficiency. Fuel 166, 219-226.
697 Bikkina, P.K., 2011. Contact angle measurements of CO2–water–quartz/calcite systems in the
698 perspective of carbon sequestration. International Journal of Greenhouse Gas Control 5, 1259-1271.
699 Busch, A., Müller, N., 2011. Determining CO2/brine relative permeability and capillary threshold
700 pressures for reservoir rocks and caprocks: Recommendations for development of standard laboratory
701 protocols. Energy Procedia 4, 6053-6060.
702 Cao, S.C., Dai, S., Jung, J., 2016. Supercritical CO2 and brine displacement in geological carbon
703 sequestration: Micromodel and pore network simulation studies. International Journal of Greenhouse
704 Gas Control 44, 104-114.
705 Chalbaud, C.A., Lombard, J.-M.N., Martin, F., Robin, M., Bertin, H.J., Egermann, P., 2007. Two Phase
706 Flow Properties of Brine-CO2 Systems in a Carbonate Core: Influence of Wettability on Pc and kr,
707 SPE/EAGE Reservoir Characterization and Simulation Conference. Society of Petroleum Engineers.
708 Chang, C., Zhou, Q., Xia, L., Li, X., Yu, Q., 2013. Dynamic displacement and non-equilibrium
709 dissolution of supercritical CO2 in low-permeability sandstone: An experimental study. International
710 Journal of Greenhouse Gas Control 14, 1-14.
711 Chatzis, I., Morrow, N.R., 1984. Correlation of capillary number relationships for sandstone. Society of
712 Petroleum Engineers Journal 24, 555-562.
713 Chiquet, P., Broseta, D.F., Thibeau, S., Capillary alteration of shaly caprocks by carbon dioxide, In
714 Proceedings of the SPE Europec/EAGE Annual Conference. Society of Petroleum Engineers: Houston,
715 TX, USA, 2005., Madrid, Spain, 13–16 June 2005.
716 Chiquet, P., Daridon, J.-L., Broseta, D., Thibeau, S., 2007. CO2/water interfacial tensions under pressure
717 and temperature conditions of CO2 geological storage. Energy Conversion and Management 48, 736-
718 744.
719 Chukwudeme, E.A., Hamouda, A.A., 2009. Enhanced oil recovery (EOR) by miscible CO2 and water
720 flooding of asphaltenic and non-asphaltenic oils. Energies 2, 714-737.
721 Cinar, Y., Riaz, A., 2014. Carbon dioxide sequestration in saline formations: Part 2—Review of
722 multiphase flow modeling. Journal of Petroleum Science and Engineering 124, 381-398.
723 Delshad, M., Wheeler, M.F., Kong, X., 2010. A critical assessment of CO2 injection strategies in saline
724 aquifers, SPE Western Regional Meeting. Society of Petroleum Engineers.

725 Ding, M., Kantzas, A., 2007. Capillary number correlations for gas-liquid systems. Journal of Canadian
726 Petroleum Technology 46.
727 Duan, Z., Sun, R., 2003. An improved model calculating CO2 solubility in pure water and aqueous NaCl
728 solutions from 273 to 533 K and from 0 to 2000 bar. Chemical Geology 193, 257-271.
729 Edlmann, K., Bensabat, J., Niemi, A., Haszeldine, R., McDermott, C., 2016. Lessons learned from using
730 expert elicitation to identify, assess and rank the potential leakage scenarios at the Heletz pilot CO 2
731 injection site. International Journal of Greenhouse Gas Control 49, 473-487.
732 Edlmann, K., Haszeldine, S., McDermott, C., 2013. Experimental investigation into the sealing
733 capability of naturally fractured shale caprocks to supercritical carbon dioxide flow. Environmental
734 earth sciences 70, 3393-3409.
735 Espinoza, D.N., Santamarina, J.C., 2010. Water - CO2 - mineral systems: Interfacial tension, contact
736 angle, and diffusion—Implications to CO2 geological storage. Water resources research 46.
737 Farokhpoor, R., Bjørkvik, B.J., Lindeberg, E., Torsæter, O., 2013a. CO2 Wettability Behavior During CO2
738 Sequestration in Saline Aquifer-An Experimental Study on Minerals Representing Sandstone and
739 Carbonate. Energy Procedia 37, 5339-5351.
740 Farokhpoor, R., Bjørkvik, B.J.A., Lindeberg, E., Torsæter, O., 2013b. Wettability behaviour of CO2 at
741 storage conditions. International Journal of Greenhouse Gas Control 12, 18-25.
742 Fathollahi, A., Rostami, B., 2015. Carbonated water injection: Effects of silica nanoparticles and
743 operating pressure. Can. J. Chem. Eng 93, 1949–1956.
744 Frailey, S.M., Grube, J.P., Seyler, B., Finley, R.J., Investigation of liquid CO2 sequestration and EOR in
745 low temperature oil reservoirs in the Illinois basin, SPE/DOE Symposium on Improved Oil Recovery.
746 Society of Petroleum Engineers: Houston, TX, USA, 2004., Tulsa, OK, USA, 17–21 April 2004.
747 Fulcher Jr, R.A., Ertekin, T., Stahl, C., 1985. Effect of capillary number and its constituents on two-phase
748 relative permeability curves. Journal of Petroleum Technology 37, 249-260.
749 Georgiadis, A., Maitland, G., Trusler, J.M., Bismarck, A., 2010. Interfacial tension measurements of the
750 (H2O+ CO2) system at elevated pressures and temperatures. Journal of Chemical & Engineering Data
751 55, 4168-4175.
752 Gozalpour, F., Ren, S., Tohidi, B., 2005. CO2 EOR and storage in oil reservoir. Oil & gas science and
753 technology 60, 537-546.
754 Gunde, A.C., Bera, B., Mitra, S.K., 2010. Investigation of water and CO2 (carbon dioxide) flooding using
755 micro-CT (micro-computed tomography) images of Berea sandstone core using finite element
756 simulations. Energy 35, 5209-5216.
757 Han, F., Busch, A., van Wageningen, N., Yang, J., Liu, Z., Krooss, B.M., 2010. Experimental study of gas
758 and water transport processes in the inter-cleat (matrix) system of coal: anthracite from Qinshui Basin,
759 China. International Journal of Coal Geology 81, 128-138.
760 Hangx, S., van der Linden, A., Marcelis, F., Bauer, A., 2013. The effect of CO2 on the mechanical
761 properties of the captain sandstone: geological storage of CO2 at the Goldeneye field (UK).
762 International Journal of Greenhouse Gas Control 19, 609-619.
763 Heaviside, J., Black, C., 1983. Fundamentals of relative permeability: experimental and theoretical
764 considerations, SPE Annual Technical Conference and Exhibition. Society of Petroleum Engineers.
765 Herring, A.L., Andersson, L., Newell, D., Carey, J., Wildenschild, D., 2014a. Pore-scale observations of
766 supercritical CO2 drainage in Bentheimer sandstone by synchrotron x-ray imaging. International
767 Journal of Greenhouse Gas Control 25, 93-101.
768 Herring, A.L., Andersson, L., Newell, D., Carey, J., Wildenschild, D., 2014b. Pore-scale observations of
769 supercritical CO 2 drainage in Bentheimer sandstone by synchrotron x-ray imaging. International
770 Journal of Greenhouse Gas Control 25, 93-101.
771 Hildenbrand, A., Schlömer, S., Krooss, B., 2002. Gas breakthrough experiments on fine - grained
772 sedimentary rocks. Geofluids 2, 3-23.
773 Iglauer, S., Mathew, M.S., Bresme, F., 2012. Molecular dynamics computations of brine-CO2 interfacial
774 tensions and brine-CO2-quartz contact angles and their effects on structural and residual trapping
775 mechanisms in carbon geo-sequestration. J Colloid Interface Sci 386, 405-414.

776 Islam, A., Chevalier, S., Sassi, M., 2013. Experimental and Numerical Studies of CO2 Injection Into
777 Water-Saturated Porous Medium: Capillary to Viscous to Fracture Fingering Phenomenon. Energy
778 Procedia 37, 5511-5519.
779 Jiang, L., Yu, M., Liu, Y., Yang, M., Zhang, Y., Xue, Z., Suekane, T., Song, Y., 2017. Behavior of
780 CO2/water flow in porous media for CO2 geological storage. Magnetic Resonance Imaging 37, 100-106.
781 Jobard, E., Sterpenich, J., Pironon, J., Corvisier, J., Jouanny, M., Randi, A., 2013. Experimental simulation
782 of the impact of a thermal gradient during geological sequestration of CO2: The COTAGES experiment.
783 International Journal of Greenhouse Gas Control 12, 56-71.
784 Kaveh, N.S., Wolf, K., Ashrafizadeh, S., Rudolph, E., 2012. Effect of coal petrology and pressure on
785 wetting properties of wet coal for CO2 and flue gas storage. International Journal of Greenhouse Gas
786 Control 11, S91-S101.
787 Kazemifar, F., Blois, G., Kyritsis, D.C., Christensen, K.T., 2015. Quantifying the flow dynamics of
788 supercritical CO2–water displacement in a 2D porous micromodel using fluorescent microscopy and
789 microscopic PIV. Advances in Water Resources.
790 Krevor, S., Blunt, M.J., Benson, S.M., Pentland, C.H., Reynolds, C., Al-Menhali, A., Niu, B., 2015.
791 Capillary trapping for geologic carbon dioxide storage–From pore scale physics to field scale
792 implications. International Journal of Greenhouse Gas Control 40, 221-237.
793 Krevor, S., Pini, R., Benson, S.M., 2013. Measurement of the multiphase flow properties of the CO2 brine
794 system for carbon sequestration. Energy Procedia 37, 4499-4503.
795 Kwelle, S.O., 2017. Experimental studies on resistance to fluid displacement in single pores, School of
796 Engineering, Institute of Material and Process. The University of Edinburgh, Edinburgh, UK, p. 206.
797 Lassen, R.N., Plampin, M., Sakaki, T., Illangasekare, T., Gudbjerg, J., Sonnenborg, T., Jensen, K.H., 2015.
798 Effects of geologic heterogeneity on migration of gaseous CO2 using laboratory and modeling
799 investigations. IJGGC 43, 213-224.
800 Lenormand, R., Touboul, E., Zarcone, C., 1988. Numerical models and experiments on immiscible
801 displacements in porous media. Journal of Fluid Mechanics 189, 37-38.
802 Levine, J.S., Matter, J.M., Goldberg, D.S., Lackner, K.S., Supp, M.G., Ramakrishnan, T., 2011. Two phase
803 brine-CO2 flow experiments in synthetic and natural media. Energy Procedia 4, 4347-4353.
804 Li, X., 2015. Experimental Studies on Pore Wetting and Displacement of Fluid by CO2 in Porous Media.
805 The University of Edinburgh, Edinburgh, UK.
806 Li, X., Boek, E., Maitland, G.C., Trusler, J.P.M., 2012. Interfacial Tension of (Brines + CO2): (0.864 NaCl
807 + 0.136 KCl) at Temperatures between (298 and 448) K, Pressures between (2 and 50) MPa, and Total
808 Molalities of (1 to 5) mol·kg–1. Journal of Chemical & Engineering Data 57, 1078-1088.
809 Liu, N., Ghorpade, S.V., Harris, L., Li, L., Grigg, R.B., Lee, R.L., The effect of pressure and temperature
810 on brine-CO2 relative permeability and IFT at reservoir conditions, In Proceedings of theSPE Eastern
811 Regional Meeting. Society of Petroleum Engineers: Houston, TX, USA, 2010., Morgantown, WV, USA,
812 13–15 October 2010.
813 Ma, J., Petrilli, D., Manceau, J.-C., Xu, R., Audigane, P., Shu, L., Jiang, P., Le-Nindre, Y.M., 2013. Core
814 scale modelling of CO2 flowing: identifying key parameters and experiment fitting. Energy Procedia
815 37, 5464-5472.
816 Manceau, J.-C., Ma, J., Li, R., Audigane, P., Jiang, P., Xu, R., Tremosa, J., Lerouge, C., 2015. Two‐phase
817 flow properties of a sandstone rock for the CO2/water system: Core‐flooding experiments, and focus
818 on impacts of mineralogical changes. Water Resources Research 51, 2885-2900.
819 Miocic, J.M., Gilfillan, S.M., Roberts, J.J., Edlmann, K., McDermott, C.I., Haszeldine, R.S., 2016. Controls
820 on CO2 storage security in natural reservoirs and implications for CO2 storage site selection.
821 International Journal of Greenhouse Gas Control 51, 118-125.
822 Müller, N., 2011. Supercritical CO2-brine relative permeability experiments in reservoir rocks—
823 Literature review and recommendations. Transport in porous media 87, 367-383.
824 Nourpour Aghbash, V., Ahmadi, M., Evaluation of CO2-EOR and Sequestration in Alaska West Sak
825 Reservoir Using Four-Phase Simulation Model, SPE Western Regional Meeting. Society of Petroleum
826 Engineers: Houston, TX, USA, 2012., Bakersfield, CA, USA, 21–23 March 2012.

827 Nutt, C., 1982. The physical basis of the displacement of oil from porous media by other fluids: a
828 capillary bundle model, Proceedings of the Royal Society of London A: Mathematical, Physical and
829 Engineering Sciences. The Royal Society, pp. 155-178.
830 Ott, H., de Kloe, K., Marcelis, F., Makurat, A., 2011. Injection of supercritical CO2 in brine saturated
831 sandstone: pattern formation during salt precipitation. Energy Procedia 4, 4425-4432.
832 Ott, H., Pentland, C., Oedai, S., 2015. CO2–brine displacement in heterogeneous carbonates.
833 International Journal of Greenhouse Gas Control 33, 135-144.
834 Peace software, 2017.
835 Pentland, C., El-Maghraby, R., Georgiadis, A., Iglauer, S., Blunt, M., 2011a. Immiscible displacements
836 and capillary trapping in CO2 storage. Energy Procedia 4, 4969-4976.
837 Pentland, C.H., El‐Maghraby, R., Iglauer, S., Blunt, M.J., 2011b. Measurements of the capillary
838 trapping of supercritical carbon dioxide in Berea sandstone. Geophysical Research Letters 38.
839 Perrin, J.-C., Benson, S., 2010. An experimental study on the influence of sub-core scale heterogeneities
840 on CO2 distribution in reservoir rocks. Transport in porous media 82, 93-109.
841 Perrin, J.-C., Krause, M., Kuo, C.-W., Miljkovic, L., Charoba, E., Benson, S.M., 2009. Core-scale
842 experimental study of relative permeability properties of CO2 and brine in reservoir rocks. Energy
843 Procedia 1, 3515-3522.
844 Physics, D.o., 2017. Q & A: Temperature and Water Molecules | Department of Physics | the University
845 of Illinois at Urbana-Champaign.
846 Pini, R., Krevor, S.C., Benson, S.M., 2012. Capillary pressure and heterogeneity for the CO2/water
847 system in sandstone rocks at reservoir conditions. Advances in Water Resources 38, 48-59.
848 Plug, W.-J., Bruining, J., 2007. Capillary pressure for the sand–CO2–water system under various
849 pressure conditions. Application to CO2 sequestration. Advances in Water Resources 30, 2339-2353.
850 Qi, R., Laforce, T., Blunt, M., 2010. Carbon Dioxide (CO2) Injection Design to Maximize Underground
851 Reservoir Storage and Enhanced Oil Recovery (EOR). Developments and Innovation in Carbon Dioxide
852 (CO2) Capture and Storage Technology (Ed. MM Maroto-Valer), Woodhead Publishing Series in
853 Energy, Oxford, 169-184.
854 Rathnaweera, T., Ranjith, P., Perera, M., 2015. Effect of salinity on effective CO2 permeability in
855 reservoir rock determined by pressure transient methods: An experimental study on Hawkesbury
856 sandstone. Rock Mechanics and Rock Engineering 48, 2093-2110.
857 Rezaei, N., Firoozabadi, A., 2014. Pressure evolution and production performance of waterflooding in
858 n-heptane-saturated fired Berea cores. SPE Journal 19, 674-686.
859 Roof, J., 1970. Snap-off of oil droplets in water-wet pores. Society of Petroleum Engineers Journal 10,
860 85-90.
861 Rostami, B., Kharrat, R., Ghotbi, C., Tabatabaie, S., 2010. Gas-oil relative permeability and residual oil
862 saturation as related to displacement instability and dimensionless numbers. Oil & Gas Science and
863 Technology–Revue de l'Institut Français du Pétrole 65, 299-313.
864 Saeedi, A., Rezaee, R., Evans, B., Clennell, B., 2011. Multiphase flow behaviour during CO2 geo-
865 sequestration: Emphasis on the effect of cyclic CO2–brine flooding. Journal of Petroleum Science and
866 Engineering 79, 65-85.
867 Sakurovs, R., Lavrencic, S., 2011. Contact angles in CO2-water-coal systems at elevated pressures.
868 International Journal of Coal Geology 87, 26-32.
869 Salimi, H., Wolf, K.-H., Bruining, J., 2012. The influence of capillary pressure on the phase equilibrium
870 of the CO2–water system: Application to carbon sequestration combined with geothermal energy.
871 International Journal of Greenhouse Gas Control 11, S47-S66.
872 Saraji, S., Goual, L., Piri, M., Plancher, H., 2013. Wettability of supercritical carbon dioxide/water/quartz
873 systems: simultaneous measurement of contact angle and interfacial tension at reservoir conditions.
874 Langmuir: the ACS journal of surfaces and colloids 29, 6856-6866.
875 Saraji, S., Piri, M., Goual, L., 2014. The effects of SO2 contamination, brine salinity, pressure, and
876 temperature on dynamic contact angles and interfacial tension of supercritical CO2/brine/quartz
877 systems. International Journal of Greenhouse Gas Control 28, 147-155.

878 Schembre, J.M., Kovscek, A.R., 2003. A technique for measuring two-phase relative permeability in
879 porous media via X-ray CT measurements. Journal of Petroleum Science and Engineering 39, 159-174.
880 Shi, J.-Q., Xue, Z., Durucan, S., 2011. Supercritical CO2 core flooding and imbibition in Tako
881 sandstone—Influence of sub-core scale heterogeneity. International Journal of Greenhouse Gas Control
882 5, 75-87.
883 Skauge, A., Håskjold, G., Thorsen, T., Aarra, M., Accuracy of gas-oil relative permeability from two-
884 phase flow experiments, In Proceedings of International Symposium of the Society of Core Analysts,
885 Calgary, AB, Canada, 7–10 September, 1997.
886 Sohrabi, M., Jamiolahmady, M., Al Quraini, A., Heavy Oil Recovery by Liquid CO2/Water Injection,
887 EUROPEC/EAGE Conference and Exhibition. Society of Petroleum Engineers: Houston, TX, USA, 2007,
888 London, UK 11–14 June 2007.
889 Song, Y., Jiang, L., Liu, Y., Yang, M., Zhao, Y., Zhu, N., Dou, B., Abudula, A., 2012. An experimental
890 study on CO2/water displacement in porous media using high-resolution magnetic resonance imaging.
891 International Journal of Greenhouse Gas Control 10, 501-509.
892 Suekane, T., Soukawa, S., Iwatani, S., Tsushima, S., Hirai, S., 2005. Behavior of supercritical CO2 injected
893 into porous media containing water. Energy 30, 2370-2382.
894 Suenaga, H., Nakagawa, K., 2011. Analysis of two-phase flow properties of sandstones to evaluate their
895 suitability for geologic storage of CO2. Energy Procedia 4, 4323-4330.
896 Trevisan, L., Pini, R., Cihan, A., Birkholzer, J.T., Zhou, Q., González - Nicolás, A., Illangasekare, T.H.,
897 2017. Imaging and quantification of spreading and trapping of carbon dioxide in saline aquifers using
898 meter - scale laboratory experiments. Water Resources Research 53, 485-502.
899 Tutolo, B.M., Luhmann, A.J., Kong, X.-Z., Saar, M.O., Seyfried, W.E., 2015. CO2 sequestration in
900 feldspar-rich sandstone: coupled evolution of fluid chemistry, mineral reaction rates, and
901 hydrogeochemical properties. Geochimica et Cosmochimica Acta 160, 132-154.
902 Wang, D., Dong, B., Breen, S., Zhao, M., Qiao, J., Liu, Y., Zhang, Y., Song, Y., 2015. Review: Approaches
903 to research on CO2/brine two-phase migration in saline aquifers. Hydrogeology Journal 23, 1-18.
904 Wang, D., Zhao, M., Song, Y., Xu, H., Ma, X., 2013. Influence of Capillary Pressure and Injection Rate
905 as well as Heterogeneous and Anisotropic Permeability on CO2 Transport and Displacement Efficiency
906 in Water-Saturated Porous Media. Energy Procedia 37, 3945-3951.
907 Xu, R., Luo, S., Jiang, P., 2011. Pore scale numerical simulation of supercritical CO2 injecting into porous
908 media containing water. Energy Procedia 4, 4418-4424.
909 Yang, D., Gu, Y., Tontiwachwuthikul, P., 2007. Wettability determination of the reservoir brine−
910 reservoir rock system with dissolution of CO2 at high pressures and elevated temperatures. Energy &
911 Fuels 22, 504-509.
912 Yu, J., Liu, N., Li, L., Lee, R.L., 2012. Generation of nanoparticle-stabilized supercritical CO2 foams,
913 Carbon Management Technology Conference. Carbon Management Technology Conference.
914 Yu, M., Song, Y., Jiang, L., Li, W., 2014. CO2/Water Displacement in Porous Medium Under Pressure
915 and Temperature Conditions for Geological Storage. Energy Procedia 61, 282-285.
916 Zhang, C., Oostrom, M., Grate, J.W., Wietsma, T.W., Warner, M.G., 2011. Liquid CO2 Displacement of
917 Water in a Dual-Permeability Pore Network Micromodel. Environmental science & technology 45,
918 7581-7588.

919